Chemical Engineering Journal 472 (2023) 144750

Contents lists available at ScienceDirect

Chemical Engineering Journal

journal homepage: www.elsevier.com/locate/cej

In-situ detection technique for charge transfer behavior of direct Z-scheme $BiVO_4$/UiO-66-NH_2 composites during photocatalytic thioanisole conversion

Xuemeng Sun [a], Jianan Liu [a], Hong Wang [a,*], Qi Li [d], Jing Zhou [e], Pengju Li [c], Ke Hu [c,*], Cheng Wang [a,b,*], Baojiang Jiang [a,*]

[a] Key Laboratory of Functional Inorganic Material Chemistry, Ministry of Education of the People's Republic of China, Heilongjiang University, Harbin 150080, PR China
[b] Jieyang Branch of Chemistry and Chemical Engineering Guangdong Laboratory, Jieyang 515200, Guangdong University of Technology, PR China
[c] Department of Chemistry, Fudan University, Shanghai 200433, PR China
[d] College of Material Science and Chemical Engineering, Harbin Engineering University, Harbin 150001, PR China
[e] Shanghai Institute of Applied Physics, Chinese Academy of Sciences, Shanghai 201800, PR China

ARTICLE INFO

Keywords:
Photocatalysis
$BiVO_4$
UiO-66-NH_2
Z-scheme heterojunction
Thioanisole oxidation

ABSTRACT

The photocatalytic efficiency can be enhanced by constructing Z-scheme heterostructures. However, there is still a lack of comprehensive and direct evidence regarding the charge transfer pathway and mode during the photocatalytic process. A composite photocatalyst $BiVO_4$/UiO-66-NH_2 (BVO/U6N) was prepared by in-situ loading $BiVO_4$ nanoparticles onto the surface of UiO-66-NH_2 using a hydrothermal method. This catalyst effectively promotes the photocatalytic conversion of thioanisole to sulfoxide. The differences between $BiVO_4$ and UiO-66-NH_2 in band structure and Fermi energy level enable the composite to act according to the Z-scheme charge transfer pattern, which significantly enhances charge separation efficiency. In-situ X-ray photoelectron spectroscopy (in-situ XPS) combined with DFT calculation confirmed the transfer of electrons from UiO-66-NH_2 to $BiVO_4$, driven by an internal electric field (IEF) upon hybridization. This demonstrates the formation of a Z-scheme photogenerated charge transfer pathway in the BVO/U6N composite. The direct Z-scheme system significantly enhances the carrier redox, resulting in a sulfoxide yield of 95.21% for the optimized sample in methanol, which is 5 times and 4.1 times higher than that of UiO-66-NH_2 and $BiVO_4$, respectively. BVO/U6N exhibits efficient photocatalysis and selectivity towards various substrate sulfides, making it a highly promising heterogeneous photocatalyst.

1. Introduction

Sulfoxide is not only extensively utilized in drug synthesis, but also serves as an indispensable bioactive component in the chemical, fine chemical and pharmaceutical industries [1,2]. Traditionally, thioanisole oxidation to sulfoxide products has been predominantly achieved through a thermal oxidation process that necessitates the use of oxidants [3,4]. However, this approach has several drawbacks, including low selectivity, high resource consumption, and the generation of highly toxic waste products [5,6]. Therefore, the quest for an eco-friendly and efficient approach to synthesizing sulfoxide has been a focal point in the field of photocatalysis research. Visible-light-driven photocatalysis is regarded as one of the most promising solutions for oxidizing thioanisole into sulfoxide, owing to its high sustainability and environmental compatibility [7–10]. At present, because of its high surface area and porous structure, COF have been widely used in photocatalytic thioanisole conversion reactions, and have made great progress [11–14]. However, due to the limited stability of COF, complex preparation methods and high cost, its application in the reaction is limited. Compared with COF, MOFs not only possess a large specific surface area and porous structure but also exhibit the advantages of facile preparation, high stability, and low cost [15–19]. Therefore, the use of MOF-based solar energy photocatalyst to promote thioanisole yield under mild conditions (ambient temperature and pressure) for further

* Corresponding authors at: Key Laboratory of Functional Inorganic Material Chemistry, Ministry of Education of the People's Republic of China, Heilongjiang University, Harbin 150080, PR China (C. Wang).
E-mail addresses: wanghong1@hlju.edu.cn (H. Wang), khu@fudan.edu.cn (K. Hu), wangc_93@gdut.edu.cn (C. Wang), jbj@hlju.edu.cn (B. Jiang).

https://doi.org/10.1016/j.cej.2023.144750
Received 11 May 2023; Received in revised form 29 June 2023; Accepted 9 July 2023
Available online 22 July 2023

synthesis of sulfoxide products is considered a highly promising approach.

Metal-Organic Frameworks (MOFs) exhibit exceptional structural and functional versatility, as well as high surface area and porosity, rendering them highly promising for a wide range of applications in catalysis, gas adsorption, chemical sensing [19–27]., and biomedicine [28–30]. However, the photocatalytic capacity of MOFs is severely limited in some oxidation reactions due to their weak response to visible light and the possible recombination of photoinduced carriers [31]. $BiVO_4$ is a highly attractive photocatalytic material due to its strong sunlight absorption and narrow band gap width [45–47]. However, due to the low conduction band (CB) level of $BiVO_4$, electron-hole separation and utilization efficiency are not optimal, resulting in unsatisfactory photocatalytic activity [48-51]. The improved photocatalytic activity can be attributed to the formation of heterojunctions, which effectually inhibits the recombination of photogenerated electron-hole pairs [32–35]. Owing to the successful transfer of photogenerated carriers at the interface, Z-scheme heterojunction can effectively mitigate electron-hole recombination and maintain high oxidation and reduction activities in both valence and conduction bands [36–40]. The efficiency of photocatalytic reactions can be enhanced by rationally designing and constructing Z-scheme heterostructures to accelerate charge separation and transfer [41–44]. The Fermi energy level difference between MOF and $BiVO_4$ generates a built-in electric field at the interface, which facilitates carrier migration between MOF and $BiVO_4$ through efficient electron transfer. Therefore, it is anticipated that a precisely engineered catalyst incorporating both UiO-66-NH_2 and $BiVO_4$ to form a Z-scheme heterostructure would effectively catalyze the oxidation of thioanisole under visible light irradiation.

We have synthesized a photocatalyst, $BiVO_4$/UiO-66-NH_2 (BVO/U6N), with a Z-scheme charge transfer process by in situ growing $BiVO_4$ on the surface of UiO-66-NH_2. This rational design not only maintains the excellent visible light response of $BiVO_4$, but also promotes the dispersion of $BiVO_4$ on the MOF surface due to the high surface area of UiO-66-NH2, providing more adsorption sites and photocatalytic reaction centers for efficient photocatalytic yield of sulfoxide. DFT calculation and in-situ XPS were used to validate the electron transfer modes of the composites, confirming the optimized BVO/U6N followed a Z-scheme electron transfer pattern, resulting in significantly improved photogenerated carrier migration and separation efficiency. The results indicate that the BVO/U6N composite shows good photocatalytic performance for the yield of sulfoxide under certain conditions. The highest photocatalysis yield rate reached 95.21%, which was 5 times and 4 times obtained using the pure UiO-66-NH_2 and $BiVO_4$, respectively.

2. Experimental section

2.1. Synthesis of UiO-66-NH_2

The synthesis of UiO-66-NH_2 was referred to the previous literature [52]. Briefly, Loaded $ZrCl_4$ (1.9 g) and NH_2-BDC (1.5 g) into a 100 mL beaker, and add 50 mL of DMF to the beaker. After complete dissolution, stir for 30 min, then add 20 mL of acetic acid and continue stirring for 30 min. Then the mixed solution was placed in a 50 mL Teflon lined autoclave for hydrothermal reaction, and the temperature was controlled at 120 ℃ for 16 h. After cooling, it was washed approximately DMF and ethanol twice, and the sample was dried at 60 °C.

2.2. Synthesis of $BiVO_4$

The synthesis of $BiVO_4$ is similar to others. Briefly, 0.12 g Bi$(NO)_3{\cdot}5H_2O$ was dissolved in 40 mL H_2O, stirred for 10 min after dissolution, followed add 0.03 g of NH_4VO_3, was added and then was stirred for further 2 h, and then put into the Teflon-lined autoclave, kept at 160 ℃ for 12 h. After being brought down to 25 ℃, the samples were washed twice with H_2O and ethanol, and dried at 60 ℃.

2.3. Synthesis of $BiVO_4$/UiO-66-NH_2

First, 0.18 g of UiO-66-NH_2 to 70 mL of Bi$(NO)_3{\cdot}5H_2O$ aqueous solution was added 0.003 g of NH_4VO_3 after dissolution. Keep stirring for 2 h. The product was placed in a Teflon-lined autoclave for hydrothermal reaction. Keep it at 160 °C for 12 h. then wash it with water and ethanol twice, and keep it at 60 °C for 12 h. Finally get BVO/U6N mixed sample. We also prepared catalysts with different $BiVO_4$ loads, halving and doubling the amounts of Bi$(NO)_3{\cdot}5H_2O$ and NH_4VO_3, as 0.5BVO/U6N and 1.5BVO/U6N.

2.4. Photocatalytic reaction

In a typical procedure, 15 mg of the synthsized photocatalyst is added to a 3 mL methanol solution containing 0.4 mmol thioanisole and placed in a 25 mL quartz reactor. Disperse the sample and solution ultrasonically for 15 min and stir vigorously, and then keep them under an oxygen atmosphere for 10 min. Then the mixed solution was irradiated with the 300 W Xenon lamp is fitted with an AM 1.5 filter and stirred for 6 h. After the photocatalysis is completed, the reaction solution is filtered with a filter membrane. After completion, gas chromatography-mass spectrometry (GC–MS) was used to detect the solution in the reactor.

2.5. Trapping experiments for visible-light-induced active species

A certain amount of Ammonium persulphate ($(NH_4)_2S_2O_8$), 1,4-benzoquinone (BQ), *tert*-Butyl Alcohol (-BuOH), 2,2,6,6-tetramethylpiperidine-1-oxyl (TEMPO) and $CuSO_4$ were used as different scavengers to detect the effects of holes, superoxide radicals, singlet oxygen, hydroxyl radical and electrons in the photocatalytic reaction. For the quenching experiment, except for adding a certain amount of quencher to the photocatalytic reactor, the other steps are the similar as method described above.

2.6. Photoelectrochemical characterization

Photochemical measurements and electrochemistry were performed in an electrochemical workstation using a three-electrode cell (Chen-Hua, 760E). The photocatalyst-coated FTO was used as the working electrode, the Pt was used as the counter electrode, and the reference electrode is Ag/AgCl, with 0.1 M Na_2SO_4 solution as an electrolyte. The photoelectrochemical measurement and the photocatalytic performance experiment were measured using the same light source for measurement.

3. Results and discussions

3.1. Morphology and structure of BVO/U6N composites

The morphologies of UiO-66-NH_2, $BiVO_4$ and BVO/U6N samples were studied by scanning electron microscopy (SEM). The synthesized UiO-66-NH_2 exhibited an octahedral structure with a size of approximately 400 nm and a relatively smooth surface (Fig. 1a). Supporting Information Fig. S1 shows the SEM image of $BiVO_4$, which appeared as tightly aggregated fine rod-like structures. In the Supporting Information Fig. S2, the XRD test of $BiVO_4$ is presented. The XRD pattern of $BiVO_4$ corresponds well with the standard monoclinic crystal system $BiVO_4$ (JCPDS No.14–0688), indicating successful preparation and high crystallinity of the $BiVO_4$. Scheme 1 illustrates the synthesis process of BVO/U6N nanomaterials, while Fig. 1b displays their SEM image. It was observed from the figures that $BiVO_4$ particles were uniformly loaded on the surface of UiO-66-NH_2 octahedron. In addition, the size of $BiVO_4$ nanoparticles distributed on the surface of UiO-66-NH_2 was significantly smaller than that of pure $BiVO_4$. One possible explanation is that UiO-66-NH_2 improved the dispersion of $BiVO_4$ and reduced the particle size

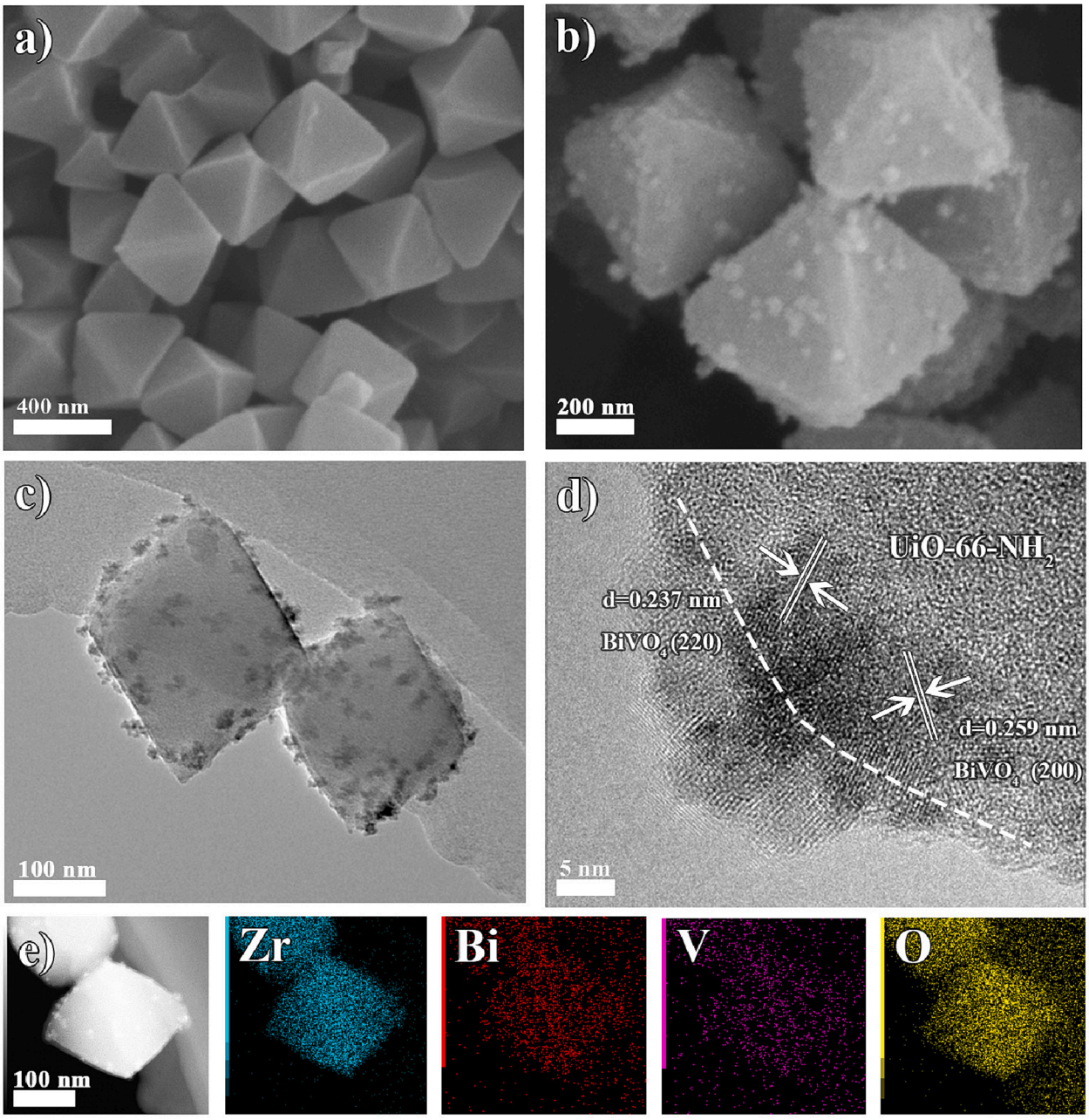

Fig. 1. a, b) SEM image of UiO-66-NH_2 and BVO/U6N composite. c, d) TEM image and HRTEM image of BVO/U6N. e) Element mapping images of Zr, Bi, V and O.

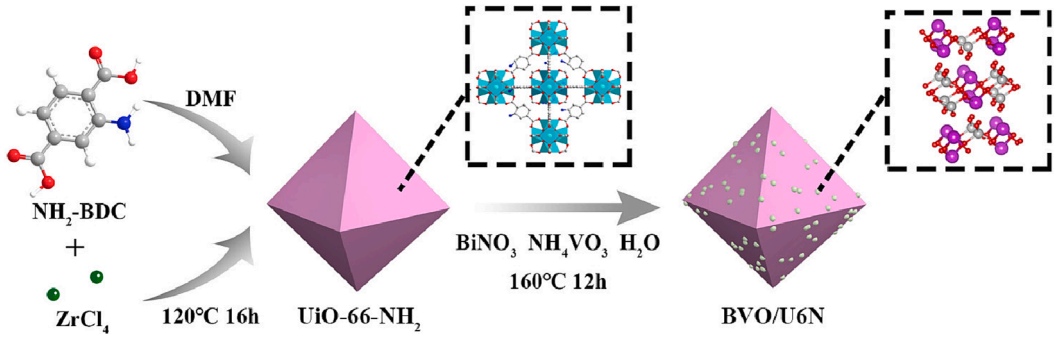

Scheme 1. Synthesis process of BVO/U6N composites.

of $BiVO_4$ nanoparticles by coordinating with functional groups to adsorb and immobilize Bi^{3+} on its surface. The generated VO_4^{3-} will be gradually bound to the immobilized Bi^{3+} on the surface of UiO-66-NH_2, preventing a large number of $BiVO_4$ nanoparticles from aggregating on the surface of UiO-66-NH_2 [53].

The microstructure and morphology of BVO/U6N samples were further investigated by transmission electron microscopy (TEM). Supporting Information Figs. S3, S4 and Fig. 1c showed TEM images of octahedral UiO-66-NH_2, $BiVO_4$ and BVO/U6N composite, respectively. The high-resolution TEM (Fig. 1d) provided direct evidence of the formation of heterogeneous interfaces between $BiVO_4$ and UiO-66-NH_2. The lattice spacing of the (220) and (200) surfaces of $BiVO_4$ was observed to be 0.237 and 0.259 nm, respectively, indicating intimate contact between $BiVO_4$ and UiO-66-NH_2 that facilitated photogenerated charge transfer. Subsequently, the elemental composition and distribution of the synthesized BVO/U6N samples were investigated through TEM-EDX elemental mapping, as illustrated in Supporting Information Fig. S5 and Fig. 1e. The obtained elemental mapping images revealed that Zr, Bi, V, C, N, and O were present in the prepared BVO/U6N composite. These findings confirmed the successful construction of BVO/U6N composite.

3.2. In-situ XPS research of BVO/U6N composites

The crystal structure and phase purity of the synthesized photocatalysts were assessed via X-ray diffraction (XRD). As shown in Fig. 2a, UiO-66-NH_2, $BiVO_4$, and BVO/U6N exhibited distinct crystal structures. The XRD results indicated that both UiO-66-NH_2 and $BiVO_4$ maintained their characteristic diffraction peaks after compounding, indicating successful completion of the process without altering their original crystal structures. The Brunauer-Emmett-Teller (BET) surface area of UiO-66-NH_2 decreases with the loading of $BiVO_4$, which is due to the small specific surface area of $BiVO_4$ (Supporting Information Fig. S6). The surface chemical states and elemental compositions of UiO-66-NH_2, $BiVO_4$, and BVO/U6N hybrids were analyzed using X-ray photoelectron spectroscopy (XPS). The Zr 3d binding energies of UiO-66-NH_2 were observed at 185.13 eV and 182.77 eV, respectively (Fig. 2b). The two binding energies of $BiVO_4$ at 159.09 and 164.39 eV corresponded to Bi $4f_{7/2}$ and Bi $4f_{5/2}$ (Fig. 2c), respectively. Additionally, the V 4p binding energies of pristine $BiVO_4$ were located at 524.11 and 516.62 eV (Fig. 2d). The shift in binding energy reflects the gain and loss of electrons between the two semiconductors, with positive and negative shifts indicating a decrease and increase in electron density, respectively. Therefore, changes in binding energy can be utilized to determine the direction of transfer for photogenerated carriers on a heterojunction photocatalyst.

We used in-situ XPS to further explore the mode of charge transfer in the BVO/U6N composite. As shown in Fig. 2b, c, compared with the pristine UiO-66-NH_2, the binding energy of Zr 3d in BVO/U6N shifted from 185.34 and 182.96 eV to 185.13 and 182.77 eV in the dark. Notably, the binding energy of Zr 3d shifted to higher energy levels in the absence of light, indicating a reduction in electron density within UiO-66-NH_2. In contrast, the binding energies of Bi 4f and V 2p for BVO/U6N exhibited significant shifts towards lower energy levels compared to those observed for $BiVO_4$ (Fig. 2c, d) [54], suggesting an increase in electron density upon contact with UiO-66-NH_2. Due to the intimate contacts and strong chemical interactions within the composite architecture, electrons residing on UiO-66-NH_2 were effectively transferred to $BiVO_4$. In-situ XPS measurements revealed that under light irradiation, the binding energy of Zr 3d in BVO/U6N composite was significantly shifted towards lower energy levels compared to its dark counterpart (Fig. 2b). However, the binding energies of Bi 4f and V 2p in the nanocomposite exhibited significant shifts towards higher energy levels (Fig. 2c, d), indicating efficient transfer of photogenerated electrons

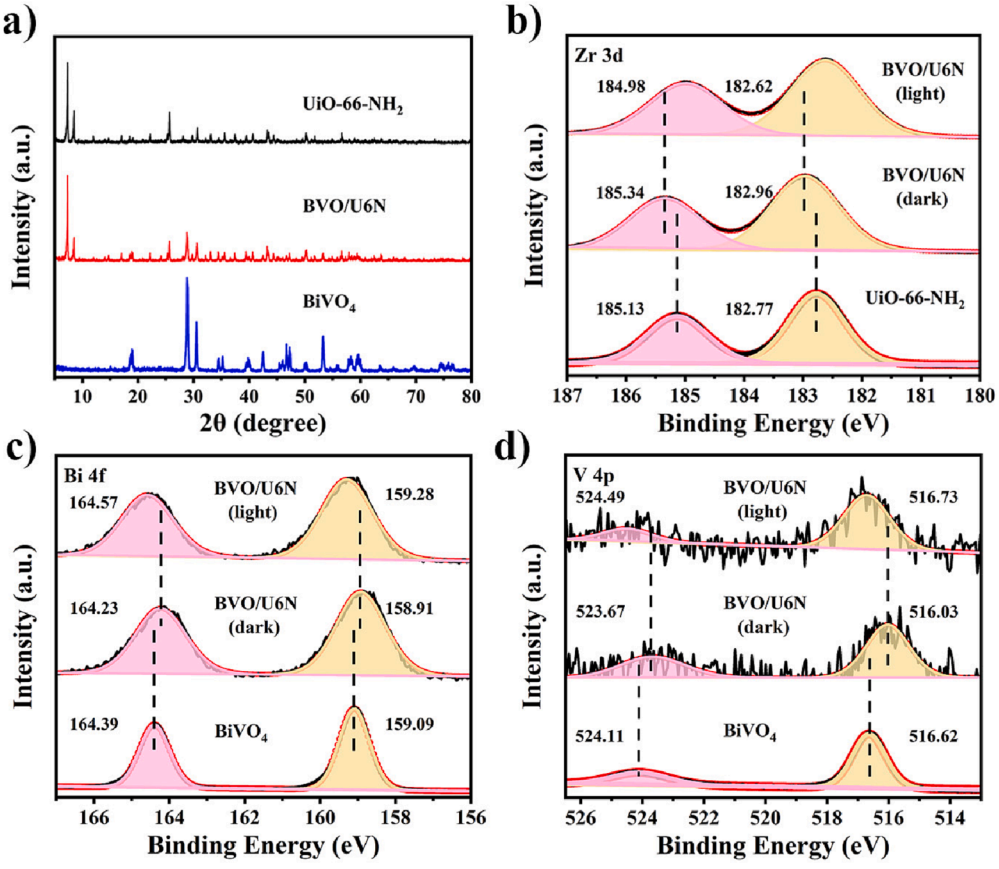

Fig. 2. (a) XRD patterns of UiO-66-NH_2, $BiVO_4$ and BVO/U6N. (b-d) In-situ XPS spectra of Zr 3d, Bi 4f, and V 4p of samples.

from $BiVO_4$ to UiO-66-NH_2 [55]. In conclusion, these XPS test results provide crucial evidence for carrier transfer at the BVO/U6N heterojunction interface under light irradiation.

3.3. Band structure and construction of Z-scheme system

The optical properties of the composites were expressed by UV–visible absorption spectra (Fig. 3a). Compared with UiO-66- NH_2, the BVO/U6N composite exhibited significantly enhanced visible-range absorption, which can be attributed to the increased photoresponse of $BiVO_4$ on the surface of UiO-66-NH_2. The correlation between $(\alpha h\nu)^2$ and $h\nu$ of $BiVO_4$ and UiO-66-NH_2 is illustrated in Supporting Information Fig. S7. By means of Kubelka-Munk transformation, the bandgap energy values for $BiVO_4$ and UiO-66-NH_2 are determined to be 2.49 eV and 2.88 eV, respectively.

Since the interfacial charge transfer process was close relevant to the work functions (WFs) of the sample, the work functions(Φ) of UiO-66-NH_2 and $BiVO_4$ were calculated using DFT, the Φ values for UiO-66-NH_2 and $BiVO_4$ are 4.63 eV and 6.25 eV respectively. When $BiVO_4$ is loaded on the UiO-66-NH_2 surface, free electrons would be transferred from the higher (UiO-66-NH_2) to the lower Fermi energy level ($BiVO_4$) until the Fermi energy levels aligned, which will induce a built electric field at the contact interface from UiO-66-NH_2 towards $BiVO_4$ [56,57]. Meanwhile, Mott-Schottky was used to measure the CB positions of $BiVO_4$ and UiO-66-NH_2. As can be seen in Fig. 3d and 3e, Mott-Schottky plots shows a positive slope, which is a characteristic of typical n-type semiconductors. The flat-band potentials of $BiVO_4$ and UiO-66-NH_2 obtained from the intersection points were 0.30 V (vs RHE) and −0.39 V (vs RHE), respectively. Considering that the CB potential of n-type semiconductors was almost equal to the flat band potential, we can determine that the conduction positions of BiVO4 and UiO-66-NH_2 were roughly 0.30 V (vs RHE) and −0.39 V (vs RHE). By combining UV and flat band potential, the band structure of $BiVO_4$ and UiO-66-NH_2 was finally obtained, as shown in Fig. 3f.

By integrating the test results of ISI-XPS, DFT calculation and band structure, we can elucidate the electron transfer mechanism of BVO/U6N (Fig. 4). Upon contact between UiO-66-NH_2 and $BiVO_4$, free electrons with higher Fermi energy on UiO-66-NH_2 migrate to $BiVO_4$ through the interface to achieve Fermi energy equilibrium. Simultaneously, an electron depletion layer is formed in UiO-66-NH_2 while an electron accumulation layer is generated in $BiVO_4$. The contact interface between UiO-66-NH_2 with positive charge and $BiVO_4$ with negative charge induces an internal electric field, resulting in the band bending of both materials. Upon light irradiation, photoexcited electron-hole pairs are generated in both $BiVO_4$ and UiO-66-NH_2. These carriers are then transferred from the conduction band of $BiVO_4$ to the HOMO energy level of UiO-66-NH_2 through interfacial band bending and the internal electric field [58–60]. This is a direct Z-scheme electron transfer mode, which was also confirmed by in situ XPS results.

Charge separation of a photocatalyst is a critical factor affecting its photoactivity. SS-SPS responses for UiO-66-NH_2 and BVO/U6N materials were conducted to investigate the charge separation of materials. As shown in Fig. 5a, the SPS response of UiO-66-NH_2 was negligible due to the rapid recombination of carriers. In contrast, the BVO/U6N nanocomposite exhibited a significant SS-SPS signal, indicating that the preparation of heterojunctions facilitated charge separation [61,62]. In addition, the amount of hydroxyl radicals formed in the photocatalytic system can be measured by coumarin method to determine photogenerate charge separation. The hydroxyl radicals were quantified by adding the probe molecule coumarin to generate luminescent 7-hydroxycoumarin molecules. Therefore, higher fluorescence intensity means more hydroxyl radicals were produced, which shows better charge separation effect. As shown in Fig. 5b, the signal of BVO/U6N was significantly stronger than that of $BiVO_4$ and UiO-66-NH_2, indicating that BVO/U6N had higher efficiency in photogenerated charge separation, which corresponds of the results of SS-SPS.

Then, the charge transfer and separation efficiency of the samples were investigated by photoelectrochemical characterization measurement techniques. As depicted in Fig. 5c, the photocurrent response of BVO/U6N was superior to that of $BiVO_4$ and UiO-66-NH_2, indicating its higher efficiency in charge separation. Nyquist plots were presented in Fig. 5d for $BiVO_4$, UiO-66-NH_2 and BVO/U6N. The smaller arc radius

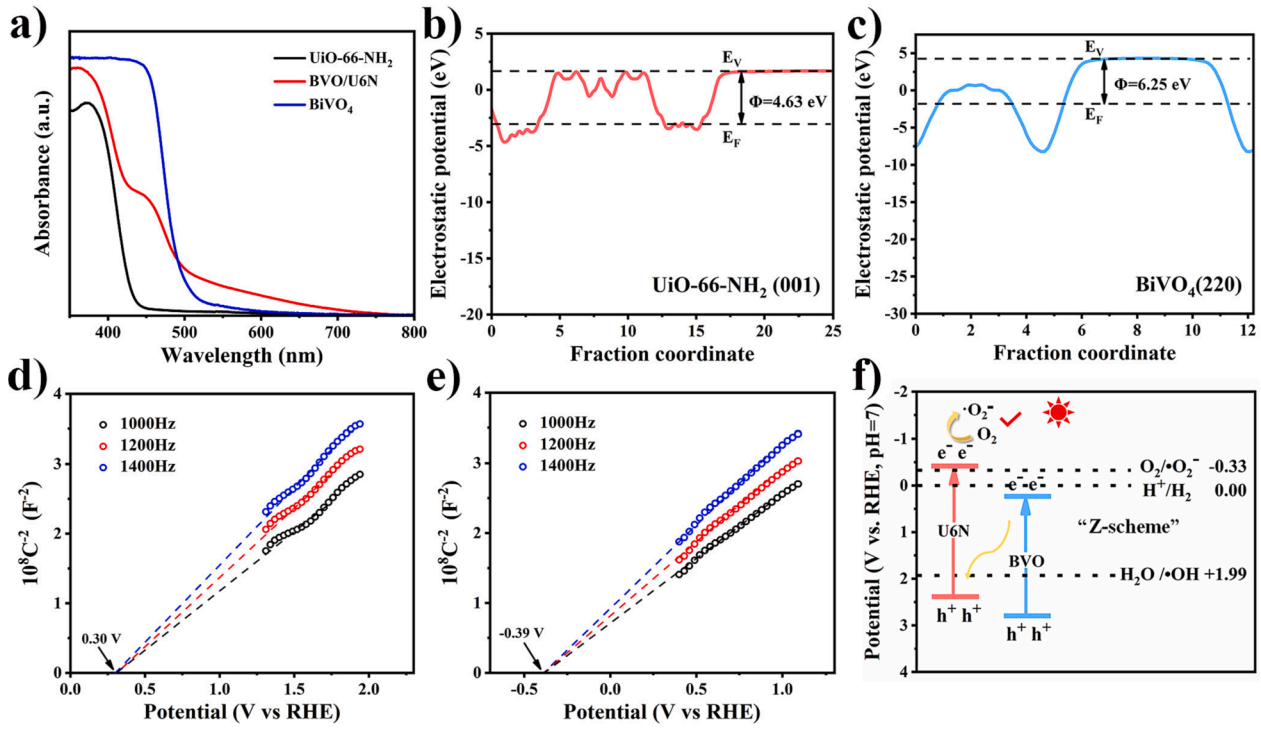

Fig. 3. (a) UV–vis absorption spectra of $BiVO_4$, UiO-66-NH_2 and BVO/U6N. (b, c) Work functions of UiO-66-NH_2 (001) and $BiVO_4$ (220). (d, e) Mott-Schottky plots of $BiVO_4$ and UiO-66-NH_2 at various frequencies. (f) Band structure alignments for BiVO4 and UiO-66-NH_2.

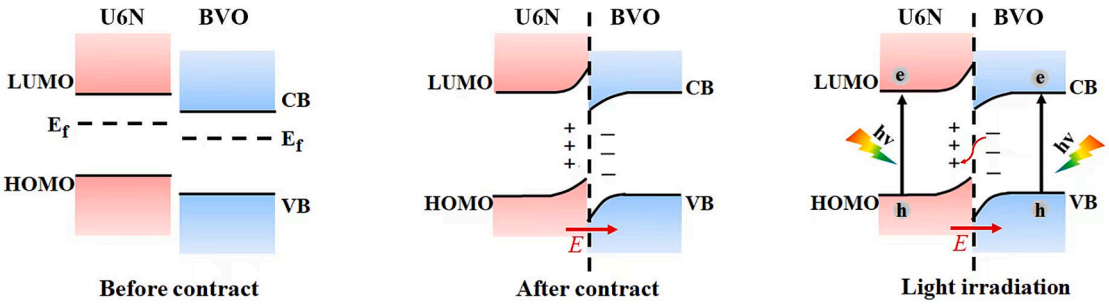

Fig. 4. Charge-transfer processes in Z-scheme heterostructures: before and after contact, formation of built-in electric fields and after illumination.

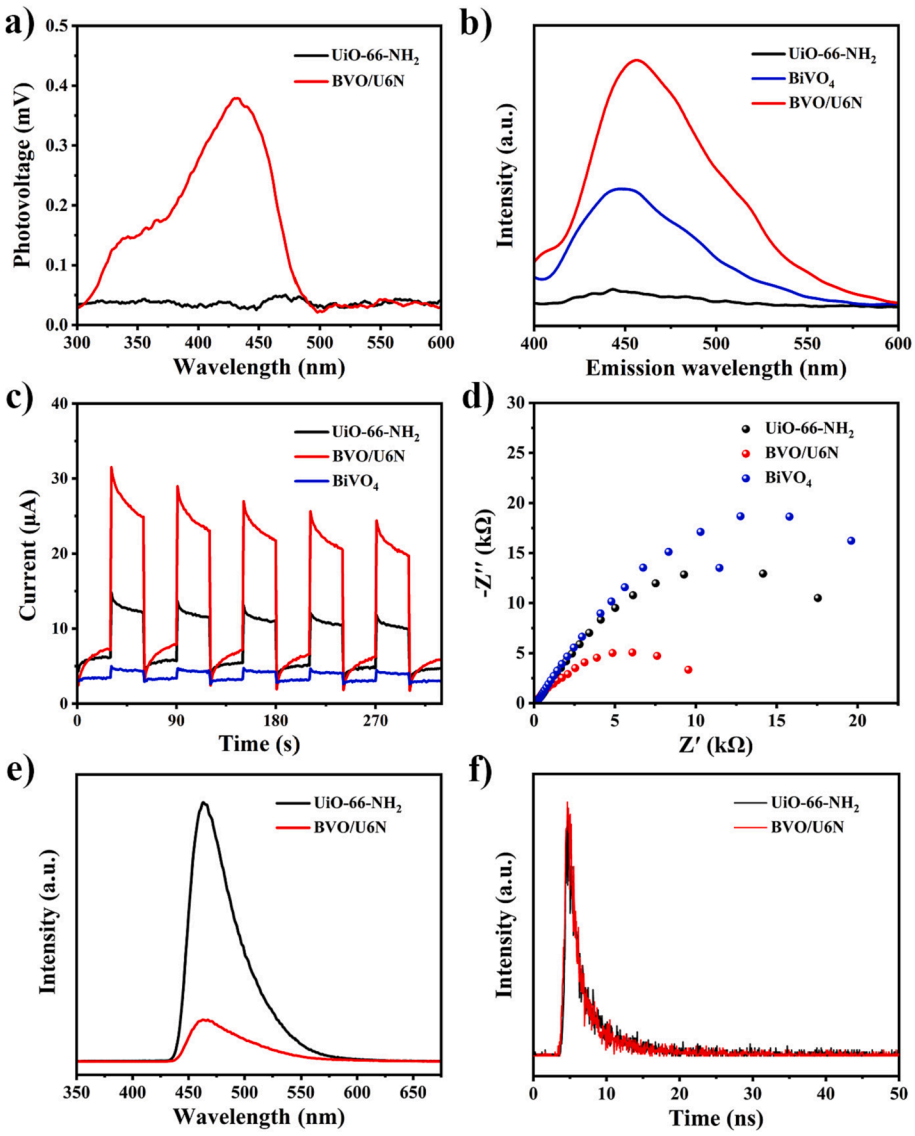

Fig. 5. (a) SS-SPS responses for UiO-66-NH_2 and BVO/U6N. (b) Fluorescence spectra of the hydroxyl radicals formed for UiO-66-NH_2, $BiVO_4$ and BVO/U6N. (c) Transient photocurrent responses and (d) EIS Nyquist plots of UiO-66-NH_2, $BiVO_4$ and BVO/U6N. (e) Steady-state PL spectra and (f) Time-resolved PL spectra of UiO-66-NH_2 and BVO/U6N.

observed for BVO/U6N indicates a reduction in interfacial charge transfer resistance, thereby facilitating the transfer of photogenerated carriers across the interface. The charge transfer kinetics of the samples were further verified using steady-state photoluminescence and time-resolved PL. In particular, PL illustrated in Fig. 5e show a significant quenching of the BVO/U6N PL intensity with the addition of $BiVO_4$, which further indicated that the Z-scheme heterostructure formed by the presence of $BiVO_4$ significantly inhibits the complexation of photo-generated electron-hole in UiO-66-NH_2. The time-resolved PL decay curves can also verify the charge transfer efficiency of these samples (Fig. 5f), identifying fluorescence lifetimes of 3.04 and 2.66 ns for UiO-66-NH_2 and BVO/U6N, respectively. It is widely acknowledged that a

shorter lifetime of time-resolved photoluminescence indicates faster transfer of photogenerated electrons in heterojunction structures. The aforementioned results demonstrate that the Z-scheme charge transfer mechanism between $BiVO_4$ and UiO-66-NH_2 exhibits higher efficiency in charge transfer and effectively suppresses electron-hole recombination.

3.4. Catalytic performance of BVO/U6N

The photocatalytic activity of the sample was assessed by selective oxidation of thioanisole to sulfoxide under AM1.5 light irradiation. $BiVO_4$, UiO-66-NH_2 and BVO/U6N were subject to photocatalytic selective oxidation of thioanisole, respectively (Fig. 6b). The yield and selectivity of sulfoxide were measured by GC–MS. As expected, both $BiVO_4$ and UiO-66-NH_2 showed low yield rates, which could be attributed to their rapid photogenerated charge carrier recombination. On the contrary, under the same reaction conditions, BVO/U6N showed the most excellent photocatalytic activity, and the yield and selectivity of sulfoxide reached 95.21% and 99.99%, respectively. As shown in Supporting Information Fig. S8, selective thioanisole oxidation to sulfoxide could be confirmed. The results indicate that the Z-scheme charge transfer mechanism of BVO/U6N significantly enhances interfacial charge separation efficiency and effectively suppresses photogenerated charge recombination, thereby demonstrating excellent photocatalytic performance. The adsorption–desorption of O_2 by photocatalyst is an important step in oxygen activation [63]. Supporting Information Fig. S9 compare an optimized models of O_2 molecules adsorbed on the surfaces of UiO-66-NH_2 and $BiVO_4$. Obviously, the adsorption energy Eads (-0.32 eV) of O_2 on UiO-66-NH_2 is higher than that on $BiVO_4$ (-0.54 eV), indicating that the O_2 adsorbed on UiO-66-NH_2 is more easily desorbed than that on $BiVO_4$, thus improving the photocatalytic performance. To further investigate the impact of solvents on this reaction (Fig. 6c), acetonitrile and DMF were employed as solvents. The results indicated that the yields and selectivities of acetonitrile and DMF were significantly inferior to those of methanol, which could be attributed to the effective hole quenching ability of methanol. This effectively inhibited electron-hole recombination, thereby retaining more e^- and $\cdot O^{2-}$.

The experiments were conducted under different time gradients (Fig. 6d). The results indicated that the yield of sulfoxide gradually accumulated with the increase of time, and reached the optimal state after 6 h. However, when the light duration reached 8 h, the yield and selectivity decreased to 79.35% and 80.24%, respectively, which may be due to the peroxidation of the thioanisole for too long a reaction time resulting in the formation of by products, such as methyl phenyl sulfone. This conclusion was proved by GC (Supporting Information Fig. S8). When the reaction is extended to 12 h, it can be found that the emergence of by-products gradually increases with the increase of time, and finally reaches a stable state (Supporting Information Fig. S11). Controlled experiments were carried out to explore the necessity of oxygen and light for the reaction. It is clear from the Supporting Information Fig. S10 that the yield of thioanisole to sulfoxide was not complete in the absence of oxygen and light. Compared with various atmospheres, it is found that the catalytic effect is best in oxygen atmosphere. This value is relatively high performance in the same type of reaction (Supporting Information Table S1). At the same time, we also carried out photocatalytic tests on UiO-66-NH_2 loaded with different contents of $BiVO_4$, and the test results showed that the photocatalytic

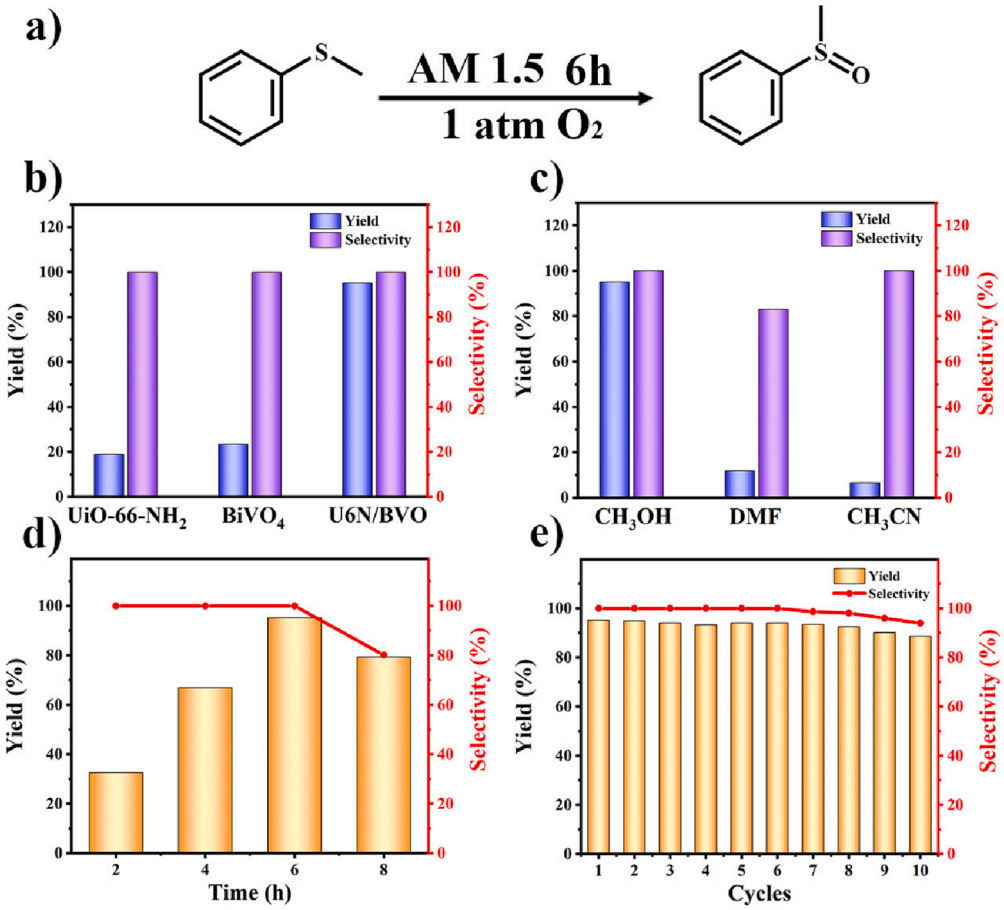

Fig. 6. (a) Photocatalytic selective oxidation of thioanisole. (b) Yield and selectivity of UiO-66-NH_2, $BiVO_4$ and BVO/U6N. (c, d) Under different solvents and times. (e) Stability test for selective oxidation of BVO/U6N with thioanisole.

performance was the best when the load of $BiVO_4$ was 10%. Too little or too much $BiVO_4$ will affect its photocatalytic activity (Supporting Information S11). In addition, the photocatalytic activity remained basically unchanged in the first 6 cycles, and the yield and selectivity of photocatalyzed thioanisole decreased slightly at the beginning of 7 cycles (Fig. 6e), which strongly indicates that the BVO/U6N heterostructure is stable for the photocatalytic yield of sulfoxide. The XRD and SEM images after the photocatalytic reaction showed no significant changed in the morphology and structure of BVO/U6N, indicating that BVO/U6N has high stability before and after the photocatalytic reaction (Supporting Information Fig. S12). At the same time, the ICP-AES test results of BVO/U6N showed that the metal content did not change significantly before and after the photocatalytic reaction, which further demonstrated the stability of the composite (Supporting Information Table S2). The electron transfer mode of the Z-scheme heterostructure can effectively inhibit the electron-hole recombination, make the electrons and holes migrate to the two ends of the composite, and improve the oxidation and reduction ability of the mixture. The relationship between conversion rate and irradiation time is shown in Supporting Information Fig. S13. The results show that the linear relationship between conversion rate and irradiation time is consistent with the first-order reaction kinetics.

The mechanism of photocatalytic selective oxidation was confirmed through a series of free radical quenching experiments (Fig. 7a). Firstly, the addition of $CuSO_4$ as an electron collector under identical reaction conditions significantly reduced the yield rate of sulfoxide, indicating that photogenerated electrons reduction triggered the radical oxidation pathway. On the contrary, the addition of $(NH_4)_2S_2O_8$ as a hole collector did not significantly alter the yield rate, implying that methanol acted as a quencher for photogenerated holes and thus hindered their participation in the oxidation process. Therefore, methanol proved to be the most satisfactory solvent for photocatalytic activity. In general hydroxyl radical (·OH), superoxide radical ($\cdot O^{2-}$) and singlet oxygen ($_1O^2$) were necessary active substances for photocatalytic reaction, because the photocatalytic reaction was carried out in methanol, which has the ability to burst holes and therefore does not produce ·OH, and therefore ·OH should not be the oxide species for the photocatalytic oxidation of thioanisole. The $\cdot O^{2-}$ and $_1O^2$ were studied by the corresponding scavenger. The addition of BQ as a $\cdot O^{2-}$ quencher resulted in a significant decrease in the yield of thioanisole, indicating that $\cdot O^{2-}$ to be pivotal in the oxidation process. In this study, when $_1O^2$ scavengers were added, there was no significant change in yield. This indicated that $_1O^2$ is not major active species in the photocatalytic oxidation of thioanisole. Therefore, the oxidation process as it stands may depend mainly on the $\cdot O^{2-}$ reactive species.

Based on the preceding discussion, a viable mechanism for charge transfer and photocatalytic oxidation in the Z-scheme system on BVO/U6N is proposed. As illustrated in Fig. 7b, $BiVO_4$ and UiO-66-NH_2 can be readily photoexcited to generate electrons and holes upon exposure to light. The photogenerated electrons in the conduction band of $BiVO_4$ are bound to the holes in the highest occupied molecular orbital level of UiO-66-NH_2, thereby inhibiting recombination between photogenerated electrons and holes within both $BiVO_4$ and UiO-66-NH_2 itself. This retention of valence band and lowest unoccupied molecular orbital levels with enhanced oxidation–reduction capacity effectively improves carrier separation efficiency and maximizes photocatalyst oxidation–reduction potential. It is worth noting that the UiO-66-NH_2 porous structure and high specific surface area provide more active and adsorption sites for thioanisole photocatalytic oxidation. The photogenerated electrons of BVO/U6N composite can effectively capture O_2 to produce $\cdot O^{2-}$, which then oxidizes sulfide to generate sulfide free radical cations. In addition, the transferred holes are heavily consumed by the primary solvent CH_3OH, producing H^+ and $\cdot CH_2OH$ for a rapid reduction of sulfide peroxide to the product sulfoxide [64–67].

Furthermore, we expanded the scope of our investigation by testing other sulfide substrates with varying substituents (Table 1) to assess the

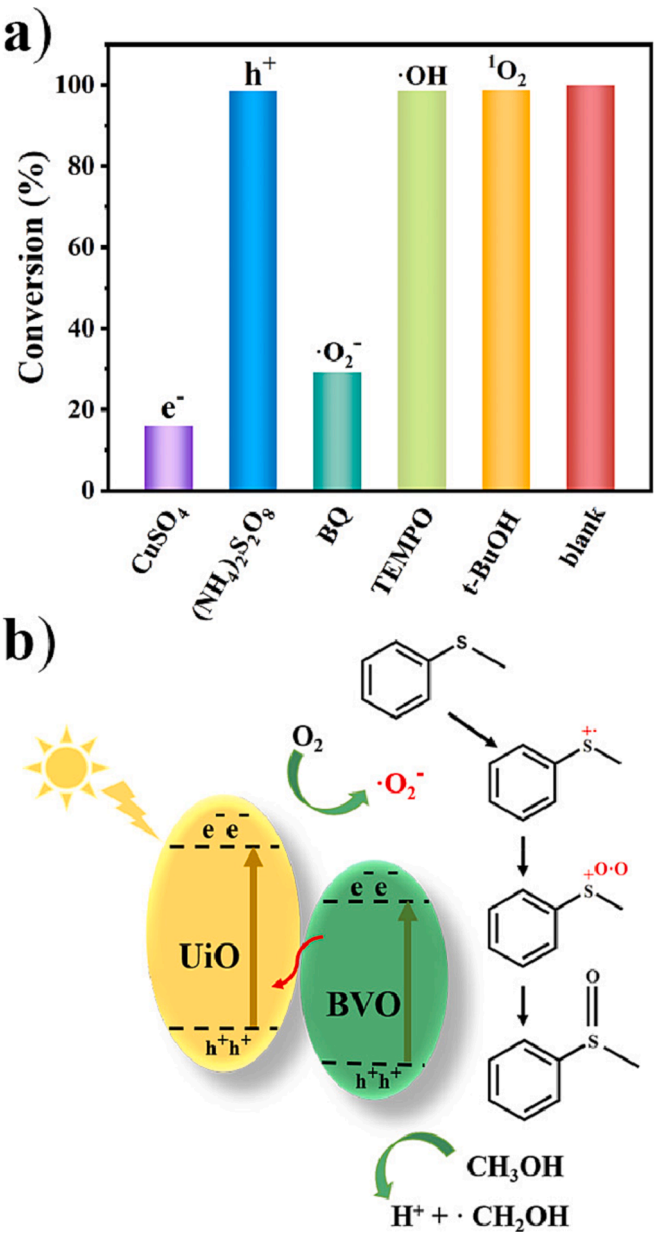

Fig. 7. (a) Photocatalytic activity tested of BVO/U6N under different quenching agents. (b) Proposed reaction mechanism of BVO/U6N photocatalytic selective oxidation of thioanisole.

generality of BVO/U6N as a photocatalyst. Specifically, we probed the impact of electron-withdrawing -F and -Cl groups as well as intersite -Br groups on the para position of thioethers. Our results demonstrate that BVO/U6N exhibits robust photocatalytic activity towards thioethers bearing diverse substituents. The results suggest that the photogenerated charge carriers in the Z-scheme system of BVO/U6N can achieve effective spatial separation and maintain strong reduction–oxidation capacity, thereby exhibiting remarkable performance in photocatalytic organic oxidation reactions.

4. Conclusion

In conclusion, the well-dispersed $BiVO_4$ was immobilized onto UiO-66-NH_2 to fabricate a BVO/U6N composite for efficient and stable photocatalytic thioanisole conversion. The UiO-66-NH_2 support significantly enhances the dispersibility of $BiVO_4$ particles, thereby exposing more adsorption and reaction sites. In-situ XPS, DFT calculation, and

Table 1
Visible light induced selective oxidation of different substrate sulfides on BVO/U6N photocatalyst.

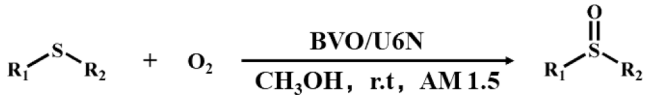

Entry	Substrate	Product	Time (h)	Yield. (%)[a]	Sel. (%)[b]
1	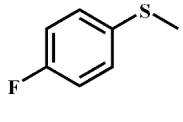	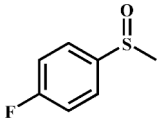	8	63.4	99.9
2			6	76.4	99.9
3	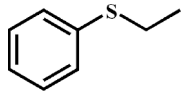	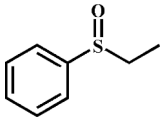	8	85.4	99.9
4	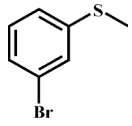	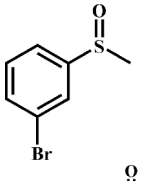	10	93.7	99.9
5	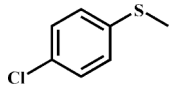	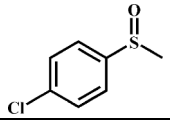	6	90.9	99.9

[a] Reaction conditions: sulfides (0.4 mmol), BVO/U6N (15 mg), CH_3OH (3.0 mL), O_2 (1 atm), the 300 W Xenon lamp is fitted with a AM1.5 filter, 25℃.
[b] Determined by GC–MS.

band structure analysis confirmed the Z-scheme electron transfer mechanism. The experimental results demonstrate that under the influence of internal electric field and interfacial band bending, photogenerated electrons are transferred from the conduction band of $BiVO_4$ to the HOMO level of UiO-66-NH_2, leading to a charge-separated state between the holes in the valence band of $BiVO_4$ and the electrons in the LUMO level of UiO-66-NH_2. As a result, the charge recombination process is suppressed and thus enhances photocatalytic selective thioanisole oxidation efficiency. After 6 h of AM1.5 light irradiation, the yield of sulfoxide reached 95.21% with a selectivity of 99.99%, which was 5.1 and 4.1 times higher than that of pure UiO-66-NH_2 and $BiVO_4$, respectively. This study demonstrates that designing MOF-based Z-scheme heterostructures is an effective strategy for optimizing photocatalytic organic oxidation reactions.

Declaration of Competing Interest

The authors declare that they have no known competing financial interests or personal relationships that could have appeared to influence the work reported in this paper.

Data availability

Data will be made available on request.

Acknowledgement

This work was supported by the National Natural Science Foundation of China (52273264), Outstanding Youth Fund of Heilongjiang Province (JQ 2020B002). The DFT calculations were performed on TianHe-2 at the LvLiang Cloud Computing Center of China.

Appendix A. Supplementary data

Supplementary data to this article can be found online at https://doi.org/10.1016/j.cej.2023.144750.

References

[1] X. Li, X. Ma, F. Zhang, X. Dong, X. Lang, Selective photocatalytic formation of sulfoxides by aerobic oxidation of sulfides over conjugated microporous polymers with thiazolo[5,4-d] thiazole linkage, Appl. Catal. B: Environ. 298 (2021) 120514.
[2] X. Chen, K. Deng, P. Zhou, Z. Zhang, Metal- and additive-free oxidation of sulfides into sulfoxides by fullerene-modified carbon nitride with visible-light illumination, ChemSusChem 11 (14) (2018) 2444–2452, https://doi.org/10.1002/cssc.201800450.
[3] X.N. Zou, D. Zhang, T.X. Luan, Q. Li, L. Li, P.Z. Li, Y. Zhao, Incorporating photochromic triphenylamine into a zirconium-organic framework for highly effective photocatalytic aerobic oxidation of sulfides, ACS Appl. Mater. Interfaces 13 (17) (2021) 20137–20144, https://doi.org/10.1021/acsami.1c03083.
[4] G. Sipos, E.E. Drinkel, R. Dorta, The emergence of sulfoxides as efficient ligands in transition metal catalysis, Chem. Soc. Rev. 44 (11) (2015) 3834–3860, https://doi.org/10.1039/c4cs00524d.
[5] B. Zhou, J. Song, Z. Zhang, Z. Jiang, P. Zhang, B. Han, Highly selective photocatalytic oxidation of biomass-derived chemicals to carboxyl compounds over Au/TiO_2, Green Chem. 19 (4) (2017) 1075–1081, https://doi.org/10.1039/c6gc03022j.
[6] D. Friedmann, A. Hakki, H. Kim, W. Choi, D. Bahnemann, Heterogeneous photocatalytic organic synthesis: state-of-the-art and future perspectives, Green Chem. 18 (20) (2016) 5391–5411, https://doi.org/10.1039/c6gc01582d.
[7] X. Yang, T. Liang, J. Sun, M.J. Zaworotko, Y. Chen, P. Cheng, Z. Zhang, Template-directed synthesis of photocatalyst-encapsulating metal-organic frameworks with boosted photocatalytic activity, ACS Catal. 9 (8) (2019) 7486–7493, https://doi.org/10.1021/acscatal.9b01783.
[8] H. Li, Y. Yang, C. He, L. Zeng, C. Duan, Mixed-ligand metal-organic framework for two-photon responsive photocatalytic C–N and C–C coupling reactions, ACS Catal. 9 (1) (2018) 422–430, https://doi.org/10.1021/acscatal.8b03537.
[9] D.M. Schultz, T.P. Yoon, Solar synthesis: prospects in visible light photocatalysis, Science 343 (6174) (2014) 1239176, https://doi.org/10.1126/science.1239176.
[10] Y. Que, J. Ruan, Y. Xiao, C. Feng, G. Lu, X. Huang, Fluorinated vesicles embedded with Ru-based catalysts as efficient and recyclable nanoreactors for photo-mediated aerobic oxidation, Polymer Chem. 11 (10) (2020) 1727–1734, https://doi.org/10.1039/c9py01648a.
[11] A. Gómez-Avilés, R.R. Solís, E.M. García-Frutos, J. Bedia, C. Belver, Novel isoreticular UiO-66-NH_2 frameworks by N-cycloalkyl functionalization of the 2-aminoterephtalate linker with enhanced solar photocatalytic degradation of acetaminophen, Chem. Eng. J. 461 (2023) 141889.
[12] H. Wang, J. Liu, X. Xiao, H. Meng, J. Wu, C. Guo, M. Zheng, X. Wang, S. Guo, B. Jiang, Engineering of SnO_2/TiO_2 heterojunction compact interface with efficient charge transfer pathway for photocatalytic hydrogen evolution, Chin. Chem. Lett. 34 (1) (2023) 107125.
[13] Y. Zhang, J. Qiu, B. Zhu, M.V. Fedin, B. Cheng, J. Yu, L. Zhang, ZnO/COF S-scheme heterojunction for improved photocatalytic H_2O_2 production performance, Chem. Eng. J. 444 (2022) 136584.
[14] L. Wang, J. Mao, G. Huang, Y. Zhang, J. Huang, H. She, C. Liu, H. Liu, Q. Wang, Configuration of hetero-framework via integrating MOF and triazine-containing COF for charge-transfer promotion in photocatalytic CO_2 reduction, Chem. Eng. J. 446 (2022) 137011.
[15] F. Zhang, X. Ma, X. Dong, X. Miao, X. Lang, Inserting acetylene into an olefin-linked covalent organic framework for boosting the selective photocatalytic aerobic oxidation of sulfides, Chem. Eng. J. 451 (2023) 138802.
[16] W. Sheng, X. Wang, Y. Wang, S. Chen, X. Lang, Integrating TEMPO into a metal-organic framework for cooperative photocatalysis: selective aerobic oxidation of sulfides, ACS Catal. 12 (18) (2022) 11078–11088, https://doi.org/10.1021/acscatal.2c02519.
[17] Q. Han, Y. Dong, C. Xu, Q. Hu, C. Dong, X. Liang, Y. Ding, Immobilization of metal-organic framework MIL-100(Fe) on the surface of $BiVO_4$: a new platform for enhanced visible-light-driven water oxidation, ACS Appl. Mater. Interfaces 12 (9) (2020) 10410–10419, https://doi.org/10.1021/acsami.9b21507.
[18] L. Jiao, J.Y.R. Seow, W.S. Skinner, Z.U. Wang, H.-L. Jiang, Metal–organic frameworks: structures and functional applications, Mater. Today 27 (2019) 43–68, https://doi.org/10.1016/j.mattod.2018.10.038.
[19] Y. Qian, D. Li, Y. Han, H.L. Jiang, Photocatalytic molecular oxygen activation by regulating excitonic effects in covalent organic frameworks, J. Am. Chem. Soc. 142 (49) (2020) 20763–20771, https://doi.org/10.1021/jacs.0c09727.
[20] L. Shen, R. Liang, L. Wu, Strategies for engineering metal-organic frameworks as efficient photocatalysts, Chin. J. Catal. 36 (12) (2015) 2071–2088, https://doi.org/10.1016/s1872-2067(15)60984-6.
[21] R. Liang, L. Shen, F. Jing, N. Qin, L. Wu, Preparation of MIL-53(Fe)-reduced graphene oxide nanocomposites by a simple self-assembly strategy for increasing interfacial contact: efficient visible-light photocatalysts, ACS Appl. Mater. Interfaces 7 (18) (2015) 9507–9515, https://doi.org/10.1021/acsami.5b00682.

[22] C.-C. Wang, X.-H. Yi, P. Wang, Powerful combination of MOFs and C3N4 for enhanced photocatalytic performance, Appl. Catal. B: Environ. 247 (2019) 24–48, https://doi.org/10.1016/j.apcatb.2019.01.091.

[23] J. Wang, A.S. Cherevan, C. Hannecart, S. Naghdi, S.P. Nandan, T. Gupta, D. Eder, Ti-based MOFs: new insights on the impact of ligand composition and hole scavengers on stability, charge separation and photocatalytic hydrogen evolution, Appl. Catal. B: Environ. 283 (2021) 119626.

[24] X. Ren, S. Wei, Q.i. Wang, L.i. Shi, X.-S. Wang, Y. Wei, G. Yang, D. Philo, F. Ichihara, J. Ye, Rational construction of dual cobalt active species encapsulated by ultrathin carbon matrix from MOF for boosting photocatalytic H2 generation, Appl. Catal. B: Environ. 286 (2021) 119924.

[25] F. Li, D. Wang, Q.-J. Xing, G. Zhou, S.-S. Liu, Y. Li, L.-L. Zheng, P. Ye, J.-P. Zou, Design and syntheses of MOF/COF hybrid materials via postsynthetic covalent modification: an efficient strategy to boost the visible-light-driven photocatalytic performance, Appl. Catal. B: Environ. 243 (2019) 621–628, https://doi.org/10.1016/j.apcatb.2018.10.043.

[26] W. Qian, T. Song, M. Ye, X. Huang, Y. Li, B. Hao, Au-covered nanographene oxide/PEG/PAMAM for surface-enhanced Raman scattering detection, Compos. Commun. 23 (2021) 100598.

[27] W. Qian, T. Song, M. Ye, X. Huang, Y. Li, B. Hao, FITC/PEG functionalized nanographene oxide/gold nanocomposites enable efficient response to dopamine, Adv. Mater. Interfaces 9 (33) (2022) 2201611.

[28] B. Hao, T. Song, M. Ye, X. Liu, J. Qiu, X. Huang, G. Lu, W. Qian, Gold/SH-functionalized nanographene oxide/polyamidamine/poly(ethylene glycol) nanocomposites for enhanced non-enzymatic hydrogen peroxide detection, Biomater. Sci. 8 (21) (2020) 6037–6044, https://doi.org/10.1039/d0bm01286f.

[29] W. Qian, T. Song, M. Ye, X. Huang, Y. Li, B. Hao, Functionalized nanographene oxide/PEG/rhodamine B/gold nanocomposite for electrochemical determination of glucose, J. Mater. Sci. Technol. 122 (2022) 141–147, https://doi.org/10.1016/j.jmst.2022.02.013.

[30] D. Tao, Z. Wang, X. Huang, M. Tian, G. Lu, I. Manners, M.A. Winnik, C. Feng, Continuous and segmented semiconducting fiber-like nanostructures with spatially selective functionalization by living crystallization-driven self-assembly, Angew. Chem. Int. Ed. 59 (21) (2020) 8232–8239, https://doi.org/10.1002/anie.202000327.

[31] Y.u. Zhang, F. Ma, M. Ling, H. Zheng, Y. Wu, L.i. Li, In-situ constructed indirect Z-type heterojunction by plasma Bi and BiO_2-X–$Bi_2O_2CO_3$ co-modified with BiOCl@Bi–MOF for enhanced photocatalytic efficiency toward antibiotics, Chem. Eng. J. 464 (2023) 142762.

[32] L. Sun, D. Wang, Y. Li, B. Wu, Q.i. Li, C. Wang, S. Wang, B. Jiang, Fully conversing and highly selective oxidation of benzene to phenol based on MOFs-derived CuO@CN photocatalyst, Chin. Chem. Lett. 34 (4) (2023) 107490.

[33] L. Shen, R. Liang, L. Wu, Strategies for engineering metal-organic frameworks as efficient photocatalysts, Chin. J. Catal. 36 (12) (2015) 2071–2088, https://doi.org/10.1016/S1872-2067(15)60984-6.

[34] A. Chatterjee, L. Wang, P. Van Der Voort, Metal-organic frameworks in photocatalytic Z-scheme heterojunctions: an emerging technology, Chem Commun (Camb) 59 (25) (2023) 3627–3654, https://doi.org/10.1039/d2cc05819g.

[35] Q. Xu, L. Zhang, B. Cheng, J. Fan, J. Yu, S-Scheme heterojunction photocatalyst, Chem 6 (7) (2020) 1543–1559, https://doi.org/10.1016/j.chempr.2020.06.010.

[36] X. Li, C. Garlisi, Q. Guan, S. Anwer, K. Al-Ali, G. Palmisano, L. Zheng, A review of material aspects in developing direct Z-scheme photocatalysts, Mater. Today 47 (2021) 75–107, https://doi.org/10.1016/j.mattod.2021.02.017.

[37] H. Wang, L. Zhang, Z. Chen, J. Hu, S. Li, Z. Wang, J. Liu, X. Wang, Semiconductor heterojunction photocatalysts: design, construction, and photocatalytic performances, Chem. Soc. Rev. 43 (15) (2014) 5234–5244, https://doi.org/10.1039/c4cs00126e.

[38] H. Li, W. Tu, Y. Zhou, Z. Zou, Z-Scheme photocatalytic systems for promoting photocatalytic performance: recent progress and future challenges, Adv. Sci 3 (11) (2016) 1500389, https://doi.org/10.1002/advs.201500389.

[39] L. Zhang, W. Feng, B. Wang, K. Wang, F. Gao, Y. Zhao, P. Liu, Construction of dual-channel for optimizing Z-scheme photocatalytic system, Appl. Catal. B: Environ. 212 (2017) 80–88, https://doi.org/10.1016/j.apcatb.2017.04.049.

[40] Z. Long, X. Yang, X. Huo, X. Li, Q. Qi, X. Bian, Q. Wang, F. Yang, WeilunYu, L. Jiang, Bioinspired Z-scheme In_2O_3/C_3N_4 heterojunctions with tunable nanorod lengths for enhanced photocatalytic hydrogen evolution, Chem. Eng. J. 461 (2023) 141893.

[41] W. Zhao, Y. Feng, H. Huang, P. Zhou, J. Li, L. Zhang, B. Dai, J. Xu, F. Zhu, N. Sheng, D.Y.C. Leung, A novel Z-scheme Ag_3VO_4/$BiVO_4$ heterojunction photocatalyst: study on the excellent photocatalytic performance and photocatalytic mechanism, Appl. Catal. B: Environ. 245 (2019) 448–458, https://doi.org/10.1016/j.apcatb.2019.01.001.

[42] E. Jiang, N. Song, G. Che, C. Liu, H. Dong, L. Yang, Construction of a Z-scheme MoS_2/$CaTiO_3$ heterostructure by the morphology-controlled strategy towards enhancing photocatalytic activity, Chem. Eng. J. 399 (2020) 125721.

[43] G. Zhang, Z. Wang, J. Wu, Construction of a Z-scheme heterojunction for high-efficiency visible-light-driven photocatalytic CO_2 reduction, Nanoscale 13 (8) (2021) 4359–4389, https://doi.org/10.1039/d0nr08442e.

[44] X. Yan, B. Wang, J. Zhao, G. Liu, M. Ji, X. Zhang, P.K. Chu, H. Li, J. Xia, Hierarchical columnar $ZnIn_2S_4$/$BiVO_4$ Z-scheme heterojunctions with carrier highway boost photocatalytic mineralization of antibiotics, Chem. Eng. J. 452 (2023) 139271.

[45] C. Liu, H. Luo, Y.u. Xu, Z. Zhang, Q. Liang, W. Wang, Z. Chen, Synergistic cocatalytic effect of ultra-thin metal-organic framework and Mo-dopant for efficient photoelectrochemical water oxidation on $BiVO_4$ photoanode, Chem. Eng. J. 384 (2020) 123333.

[46] P.V. Hlophe, L.C. Mahlalela, L.N. Dlamini, A composite of platelet-like orientated $BiVO_4$ fused with MIL-125(Ti): synthesis and characterization, Sci. Rep. 9 (1) (2019) 10044, https://doi.org/10.1038/s41598-019-46498-w.

[47] X. Wang, Y. Wang, M. Gao, J. Shen, X. Pu, Z. Zhang, H. Lin, X. Wang, $BiVO_4$/$Bi_4Ti_3O_{12}$ heterojunction enabling efficient photocatalytic reduction of CO_2 with H_2O to CH_3OH and CO, Appl. Catal. B: Environ. 270 (2020) 118876.

[48] M. de la Garza-Galván, P. Zambrano-Robledo, J. Vazquez-Arenas, I. Romero-Ibarra, C. Ostos, J. Peral, U.M. García-Pérez, In situ synthesis of Au-decorated BiOCl/$BiVO_4$ hybrid ternary system with enhanced visible-light photocatalytic behavior, Appl. Surf. Sci. 487 (2019) 743–754, https://doi.org/10.1016/j.apsusc.2019.05.041.

[49] S. Wang, P. Chen, J.H. Yun, Y. Hu, L. Wang, An electrochemically treated $BiVO_4$ photoanode for efficient photoelectrochemical water splitting, Angew. Chem. Int. Ed. 56 (29) (2017) 8500–8504, https://doi.org/10.1002/anie.201703491.

[50] L. Wang, D. Han, S. Ni, W. Ma, W. Wang, L. Niu, Photoelectrochemical device based on Mo-doped $BiVO_4$ enables smart analysis of the global antioxidant capacity in food, Chem. Sci. 6 (11) (2015) 6632–6638, https://doi.org/10.1039/c5sc02277k.

[51] R. Li, H. Han, F. Zhang, D. Wang, C. Li, Highly efficient photocatalysts constructed by rational assembly of dual-cocatalysts separately on different facets of $BiVO_4$, Energy Environ. Sci. 7 (4) (2014) 1369–1376, https://doi.org/10.1039/c3ee43304h.

[52] J. Liu, Q. Li, X. Xiao, F. Li, C. Zhao, Q. Sun, P. Qiao, J. Zhou, J. Wu, B. Li, H. Bao, B. Jiang, Metal-organic frameworks loaded on phosphorus-doped tubular carbon nitride for enhanced photocatalytic hydrogen production and amine oxidation, J. Colloid Interface Sci. 590 (2021) 1–11, https://doi.org/10.1016/j.jcis.2021.01.031.

[53] C. Cheng, J. Fang, S. Lu, C. Cen, Y. Chen, L. Ren, W. Feng, Z. Fang, Zirconium metal-organic framework supported highly-dispersed nanosized $BiVO_4$ for enhanced visible-light photocatalytic applications, J. Chem. Technol. Biotechnol. 91 (11) (2016) 2785–2792, https://doi.org/10.1002/jctb.4885.

[54] Z. Zhang, M. Wang, Z. Chi, W. Li, H. Yu, N. Yang, H. Yu, Internal electric field engineering step-scheme–based heterojunction using lead-free Cs_3Bi_2Br 9 perovskite–modified In4SnS8 for selective photocatalytic CO2 reduction to CO, Appl. Catal. B: Environ. 313 (2022) 121426.

[55] L. Wang, B. Cheng, L. Zhang, J. Yu, In situ irradiated XPS investigation on S-scheme TiO_2@$ZnIn_2S_4$ photocatalyst for efficient photocatalytic CO_2 reduction, Small 17 (41) (2021) e2103447.

[56] J. Liu, X. Sun, B. Jiang, M. Liu, Q. Li, X. Xiao, H. Wang, M. Zheng, S. Guo, J. Wu, Y. Zhang, K. Shi, W. Zhou, UiO-66-NH_2 octahedral nanocrystals decorated with $ZnFe_2O_4$ nanoparticles for photocatalytic alcohol oxidation, ACS Appl. Nano Mater. 5 (2) (2022) 2231–2240, https://doi.org/10.1021/acsanm.1c03924.

[57] L. Bi, X. Gao, L. Zhang, D. Wang, X. Zou, T. Xie, Enhanced photocatalytic hydrogen evolution of NiCoP/g-C_3N_4 with improved separation efficiency and charge transfer efficiency, ChemSusChem 11 (1) (2018) 276–284, https://doi.org/10.1002/cssc.201701574.

[58] D. Zhao, Y. Wang, C.-L. Dong, Y.-C. Huang, J. Chen, F. Xue, S. Shen, L. Guo, Boron-doped nitrogen-deficient carbon nitride-based Z-scheme heterostructures for photocatalytic overall water splitting, Nat. Energy 6 (4) (2021) 388–397, https://doi.org/10.1038/s41560-021-00795-9.

[59] J. Low, B. Dai, T. Tong, C. Jiang, J. Yu, In situ irradiated X-ray photoelectron spectroscopy investigation on a direct Z-scheme TiO_2/CdS composite film photocatalyst, Adv. Mater. 31 (6) (2019) e1802981.

[60] Q. Li, W. Feng, Y. Liu, D. Chen, Z. Wu, H. Wang, Synergistic effect of spatially isolated Ni_2P and NiO redox cocatalysts on g-C_3N_4 for sustainably boosted CO_2 photocatalytic reduction, J. Mater. Chem. A 10 (29) (2022) 15752–15765, https://doi.org/10.1039/d2ta03095k.

[61] I. Khan, X. Chu, Y. Liu, S. Khan, L. Bai, L. Jing, Synthesis of Ni^{2+} cation modified TS-1 molecular sieve nanosheets as effective photocatalysts for alcohol oxidation and pollutant degradation, Chin. J. Catal. 41 (10) (2020) 1589–1602, https://doi.org/10.1016/s1872-2067(20)63555-0.

[62] J. Bian, Z. Zhang, J. Feng, M. Thangamuthu, F. Yang, L. Sun, Z. Li, Y. Qu, D. Tang, Z. Lin, F. Bai, J. Tang, L. Jing, Energy platform for directed charge transfer in the cascade Z-scheme heterojunction: CO2 photoreduction without a cocatalyst, Angew. Chem. Int. Ed. 60 (38) (2021) 20906–20914, https://doi.org/10.1002/anie.202106929.

[63] Z. Wang, Q. Cheng, X. Wang, J. Li, W. Li, Y. Li, G. Zhang, Carbon dots modified bismuth antimonate for broad spectrum photocatalytic degradation of organic pollutants: boosted charge separation, DFT calculations and mechanism unveiling, Chem. Eng. J. 418 (2021) 129460.

[64] X. Lan, Q. Li, Y. Zhang, Q.i. Li, L. Ricardez-Sandoval, G. Bai, Engineering donor-acceptor conjugated organic polymers with boron nitride to enhance photocatalytic performance towards visible-light-driven metal-free selective oxidation of sulfides, Appl. Catal. B: Environ. 277 (2020) 119274.

[65] X. Lang, J. Zhao, X. Chen, Visible-light-induced photoredox catalysis of dye-sensitized titanium dioxide: selective aerobic oxidation of organic sulfides, Angew. Chem. Int. Ed. 55 (15) (2016) 4697–4700, https://doi.org/10.1002/anie.201600405.

[66] H. Hao, X. Li, X. Lang, Anthraquinones as photoredox active ligands of TiO_2 for selective aerobic oxidation of organic sulfides, Appl. Catal. B: Environ. 259 (2019) 118038.

[67] A.S. Hainer, J.S. Hodgins, V. Sandre, M. Vallieres, A.E. Lanterna, J.C. Scaiano, Photocatalytic hydrogen generation using metal-decorated TiO2: sacrificial donors vs true water splitting, ACS Ener. Lett. 3 (3) (2018) 542–545, https://doi.org/10.1021/acsenergylett.8b00152.